Check for updates

Angewandte Chemie International Edition

Angewandte International Edition Chemie

How to cite: *Angew. Chem. Int. Ed.* **2026**, 65, e4237539
doi.org/10.1002/anie.4237539

RESEARCH ARTICLE

Constructing Substituted-Pyridine-Linked Conjugated Porous Polymers via Multicomponent Hantzsch-Type Reaction for Efficient Hydrogen Peroxide Photosynthesis from Real Seawater and Air

Changgui Lv[1] | Jingmin Ge[2] | Xikai Chen[1] | Jinyu Liu[1] | Yanming Zhao[1] | Abdullah M. Al-Enizi[3] | Ayman Nafady[3] | Shengqian Ma[4]

[1]Henan Institute of Advanced Technology, Zhengzhou University, Zhengzhou, China | [2]School of Mechanics and Safety Engineering, Zhengzhou University, Zhengzhou, China | [3]Department of Chemistry, College of Science, King Saud University, Riyadh, Saudi Arabia | [4]Department of Chemistry, University of North Texas, Denton, Texas, USA

Correspondence: Yanming Zhao (yanmingzhao@zzu.edu.cn) | Shengqian Ma (Shengqian.Ma@unt.edu)

Received: 13 July 2026 | **Revised:** 10 August 2026 | **Accepted:** 13 August 2026

Keywords: conjugated porous polymers | multicomponent Hantzsch reaction | photocatalytic H_2O_2 production | seawater | synergistic catalysis

ABSTRACT

Conjugated porous polymers (CPPs) have emerged as promising organo-based semiconducting materials for solar-to-chemical energy conversion due to their customizable structures and functionalities. Exploring diverse synthetic routes provides a strong driving force to promote the development of this intriguing class of photocatalysts. Herein, we report a multicomponent reaction (MCR)-based strategy to construct photoactive CPPs with precisely engineered donor–acceptor architectures. Utilizing a Hantzsch-type three-component condensation, a new family of pyridine-3,5-dicarbonitrile-linked CPPs (HCPPs) was synthesized, wherein β-ketonitrile-derived building units are strategically incorporated to generate electron-deficient heterocyclic linkages that serve as intrinsic acceptors. The resulting materials exhibit exceptional photophysical properties and enable efficient non-sacrificial hydrogen peroxide (H_2O_2) photosynthesis. Notably, HCPP-1, bearing a thiophene-based donor, achieves a remarkable H_2O_2 production rate of 5230 μmol g^{-1} h^{-1} under visible light in pure water/oxygen, and maintains high performance (4850 μmol g^{-1} h^{-1}) even under simulated sunlight using real seawater and ambient air, outperforming the vast majority of reported photocatalysts. Mechanistic studies reveal spatially separated redox centers that synergistically drive an indirect two-electron oxygen reduction reaction (ORR) and a four-electron water oxidation reaction (WOR). This MCR-enabled design opens a general avenue to functional porous semiconductors for advanced solar fuel applications.

1 | Introduction

Hydrogen peroxide (H_2O_2) is a cornerstone chemical valued for its potent oxidizing capacity and eco-friendly nature, finding extensive applications spanning chemical manufacturing to disinfection [1]. It also emerges as a promising clean energy carrier, boasting a high energy density (60wt%; 3.0 MJ L^{-1}) comparable to compressed hydrogen (2.8 MJ L^{-1} at 35 MPa) while offering superior handleability in storage and transport [2–4]. However, industrial H_2O_2 production remains dominated

These authors Changgui Lv and Jingmin Ge contributed equally to this work.

All rights reserved, including rights for text and data mining and training of artificial intelligence technologies or similar technologies.
© 2026 Wiley-VCH GmbH

by the anthraquinone process, an energy-demanding route burdened by substantial environmental drawbacks [5, 6]. In this context, artificial photosynthesis, enabling direct solar-driven H_2O_2 generation from H_2O and O_2 alone, presents a sustainable and potentially cost-effective alternative [7–11]. Although organic sacrificial agents (e.g., alcohols) are frequently employed to accelerate reaction kinetics, they complicate product purification and obscure intrinsic photocatalytic performance [9, 12, 13]. A more elegant solution involves the concurrent oxygen reduction reaction (ORR) and water oxidation reaction (WOR) within a single system, delivering an atom-economical, sacrificial-agent-free pathway [14, 15]. Thermodynamically, coupling the two-electron ($2e^-$) ORR with the four-electron ($4e^-$) WOR is favorable; moreover, O_2 and protons generated in situ by WOR can serve as essential reactants for ORR [10, 16, 17]. Nonetheless, when both half-reactions occur on identical or adjacent catalytic sites, charge recombination severely curtails efficiency. Spatial separation of redox centers is therefore imperative [9], a strategy that demands photocatalysts with precisely engineered band structures and electronic properties to enable efficient charge separation.

Polymeric photocatalysts, constructed from abundant organic building blocks through covalent linkages, provide a versatile platform for integrating spatially segregated redox-active units tailored toward H_2O_2 photosynthesis [18–20]. Among them, conjugated porous polymers (CPPs), encompassing both crystalline and amorphous architectures, stand out by virtue of their extended π-conjugation, permanent porosity, and molecular-level designability. These attributes endow CPPs with high surface areas, exceptional stability, strong visible-light absorption, and tunable optoelectronic properties, establishing them as exemplary organic semiconductor photocatalysts [21–23]. Nevertheless, their structural diversity and photocatalytic performance are often constrained by conventional synthetic methodologies that rely heavily on noble-metal-catalyzed cross-coupling reactions (e.g., Sonogashira, Suzuki–Miyaura), which not only inflate production costs but also risk residual metal contamination [24–26]. In this context, multicomponent reactions (MCRs) emerge as a compelling alternative, typically proceeding under metal-free conditions to efficiently assemble structurally complex and diverse architectures from three or more components [27–29]. This convergent approach significantly boosts synthetic efficiency while enhancing structural and functional programmability in polymer chemistry [30, 31]. Notably, when the resulting MCR-derived polymers incorporate intrinsically photoactive covalent linkages (especially heterocyclic motifs), the need for multiple photoactive monomers is reduced, thereby simplifying synthesis. Harnessing MCRs to construct functional, heterocycle-linked CPPs thus represents a highly promising and sustainable strategy for efficient, non-sacrificial H_2O_2 photosynthesis.

The Hantzsch reaction is one of the oldest and most famous MCRs, proceeding via organic acid-catalyzed cyclocondensation of three components (i.e., aldehyde, β-ketoester, and ammonium acetate) to afford 1,4-dihydropyridines (DHPs), which are readily oxidized to the corresponding pyridine derivatives (Scheme S2) [32–35]. The significance of this reaction is underscored by the multifaceted utility of its products: DHPs function not only as candidate drugs for cardiovascular diseases but also as effective reductants in photoredox catalysis, while pyridine motifs are ubiquitous scaffolds in bioactive compounds [36–39]. Despite its prominence, the applications of the Hantzsch reaction in the field of CPPs have not yet been explored. We thus envisioned that adapting this classical MCR could establish a general and robust platform for constructing photocatalytically active, substituted-pyridine-linked CPPs, thereby diversifying synthetic strategies and expanding the CPP library for photocatalytic H_2O_2 production. It is worth noting that most reported photocatalytic systems perform optimally only under pure oxygen, with significantly compromised activity in air [40, 41]. Moreover, although using seawater instead of freshwater for H_2O_2 photosynthesis could alleviate freshwater scarcity and align with sustainable development goals, the presence of various salts usually leads to severe activity suppression due to complex interfering chemistry [15, 42, 43]. Consequently, a system capable of efficiently producing H_2O_2 from seawater and air under ambient conditions, without sacrificial reagents and driven solely by light, would constitute a notable advance, seamlessly merging operational simplicity with environmental sustainability.

The strategic incorporation of donor–acceptor (D–A) motifs into π-conjugated polymers has emerged as a powerful approach to enhance charge separation and migration, thereby boosting photocatalytic efficiency [24, 40, 44]. Herein, we report the first construction of a new class of pyridine-3,5-dicarbonitrile-linked CPPs (denoted HCPPs, where "H" stands for the Hantzsch-type reaction) via a modified three-component Hantzsch reaction employing β-ketonitrile-based precursors instead of conventional β-ketoester analogues. These developed HCPPs are amorphous materials with tunable D–A architectures, specifically tailored for non-sacrificial photocatalytic H_2O_2 production. Among them, HCPP-1, comprising electron-rich thieno[3,2-b]thiophene (TT) units as donors and electron-deficient pyridine–dicarbonitrile linkages as acceptors, was selected as a representative for in-depth investigation (Figure 1). This polymer exhibits a comparable specific surface area, broad visible-light absorption, favorable hydrophilicity, and can be readily exfoliated into ultrathin nanosheets (~4.0 nm thick) by ultrasonication. Using H_2O and O_2 as feedstocks, HCPP-1 delivers an exceptional H_2O_2 evolution rate of 5230 μmol g^{-1} h^{-1} under visible light, along with a notable apparent quantum yield (AQY) of 2.14 % at a long wavelength of 650 nm and excellent recyclability, surpassing most reported catalytic systems. Combined experimental and theoretical analyses indicate that the photocatalytic pathway involves both an indirect $2e^-$ ORR localized on benzene rings adjacent to the pyridine unit and a $4e^-$ WOR occurring on the TT moieties. The spatial separation of these redox sites effectively mitigates charge recombination. Remarkably, HCPP-1 maintains a high activity of 4850 μmol g^{-1} h^{-1} even when operated under simulated sunlight using real seawater and ambient air, outperforming nearly all known photocatalysts under comparable conditions. Furthermore, the generalizability of this synthetic methodology was also validated. This work not only establishes a versatile platform for designing high-performance polymeric photocatalysts but also paves the way toward sustainable, solar-driven H_2O_2 production in natural environments.

2 | Results and Discussion

To verify the feasibility of the three-component reaction strategy, we firstly synthesized the model compound of the substituted

15213773, 2026, 42, Downloaded from https://onlinelibrary.wiley.com/doi/10.1002/anie.a237539 by Shengqian Ma - University Of North Texas Willis Library , Wiley Online Library on [21/10/2026]. See the Terms and Conditions (https://onlinelibrary.wiley.com/terms-and-conditions) on Wiley Online Library for rules of use; OA articles are governed by the applicable Creative Commons License

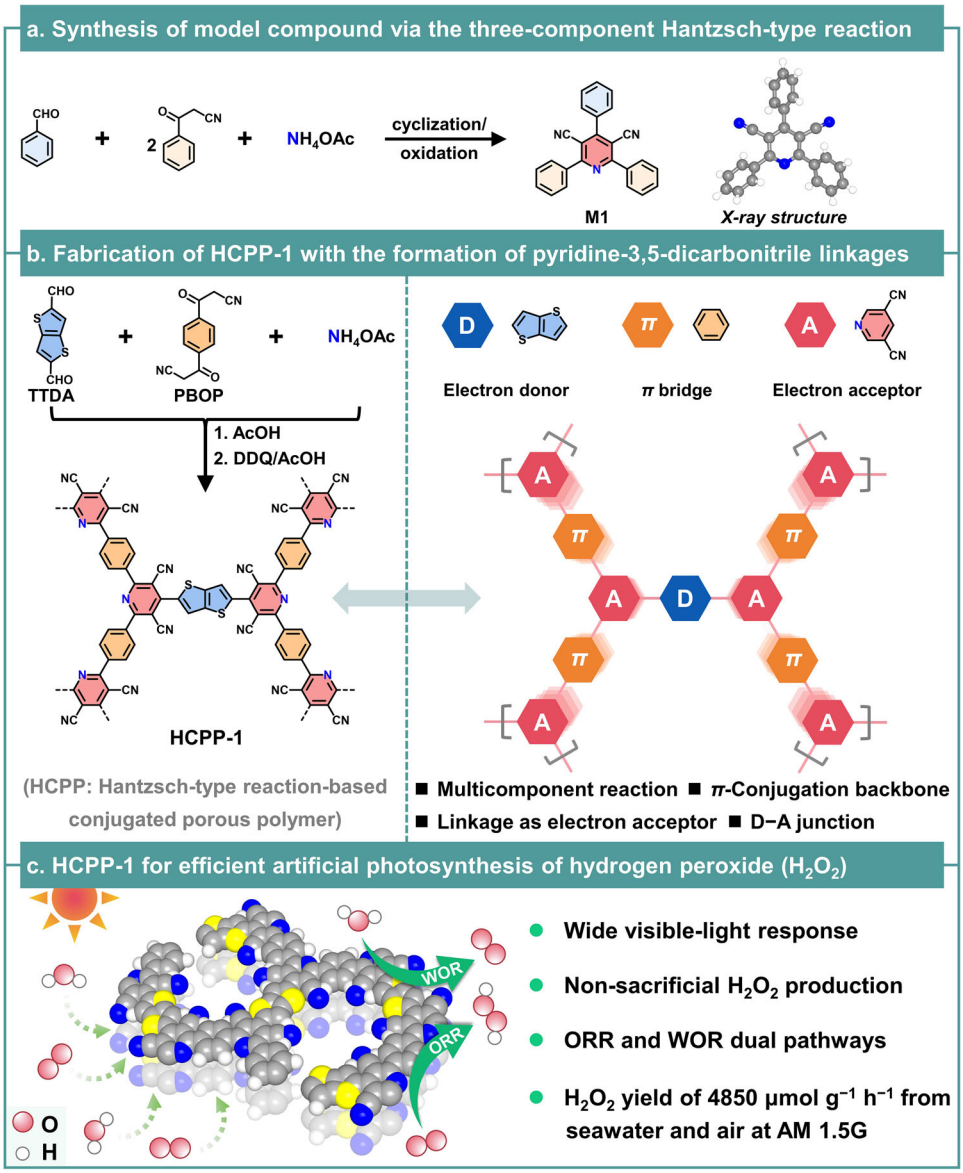


FIGURE 1 | (a) Synthesis of the model compound **M1** via a Hantzsch-type reaction and its single-crystal structure. (b) Synthetic route toward the pyridine-3,5-dicarbonitrile-linked HCCP-1 with the formation of D–A junctions. (c) Schematic diagram for HCPP-1 toward artificial photosynthesis of H_2O_2. C, N, S, H, and O are represented in gray, blue, yellow, white, and red, respectively.

pyridine **M1** via the Hantzsch-type reaction of benzoylacetonitrile, benzaldehyde, and ammonium acetate (NH_4OAc) (Figure 1a). **M1** was easily obtained under mild conditions, and its structure was unambiguously confirmed by nuclear magnetic resonance (NMR) spectroscopy, high-resolution mass spectrometry (HR-MS), and single crystal X-ray diffraction analysis (Figures S1–S3 and Table S1). The presence of two strongly electron-withdrawing cyano groups renders this pyridine-3,5-dicarbonitrile core, serving as the linkage in HCPPs, an effective electron-acceptor unit [45]. This electronic characteristic necessitates its rational pairing with an electron-rich motif to construct an efficient D–A type polymer. Thiophene-based monomers have attracted considerable interest in this context due to their strong electron-donating ability [24]. Accordingly, a novel MCR-CPP, HCPP-1, was synthesized via the three-component Hantzsch-type reaction, where 3,3′-(1,4-phenylene)bis(3-oxopropanenitrile) (PBOP), thieno[3,2-b]thiophene-2,5-dicarbaldehyde (TTDA), and NH_4OAc in acetic acid (AcOH) were first subjected to cyclocondensation at 180°C for 72 h, followed by oxidation with 2,3-dichloro-5,6-dicyano-1,4-benzoquinone (DDQ) at 110°C for 24 h, affording the target polymer (Figure 1b).

The chemical structure of HCPP-1 was initially characterized by Fourier transform infrared (FT-IR) spectroscopy. As shown in Figure 2a, the FT-IR spectrum of HCPP-1 displays characteristic signals at approximately 1551 and 2213 cm^{-1}, corresponding to the pyridyl and cyano moieties, respectively. These signals are similar to those observed for the model compound **M1**, suggesting the successful formation of the pyridine-3,5-dicarbonitrile linkage. A strong band at ~854 cm^{-1}, identical to that of the precursor TTDA, is assigned to the vibration of the thiophene-based TT unit [24]. Further structural confirmation was obtained through solid-state ^{13}C cross-polarization magic-angle-spinning (CP/MAS) NMR spectroscopy. A comparative analysis of the

15213773, 2026, 42, Downloaded from https://onlinelibrary.wiley.com/doi/10.1002/anie.4237539 by Shengqian Ma - University Of North Texas Willis Library , Wiley Online Library on [21/10/2026]. See the Terms and Conditions (https://onlinelibrary.wiley.com/terms-and-conditions) on Wiley Online Library for rules of use; OA articles are governed by the applicable Creative Commons License

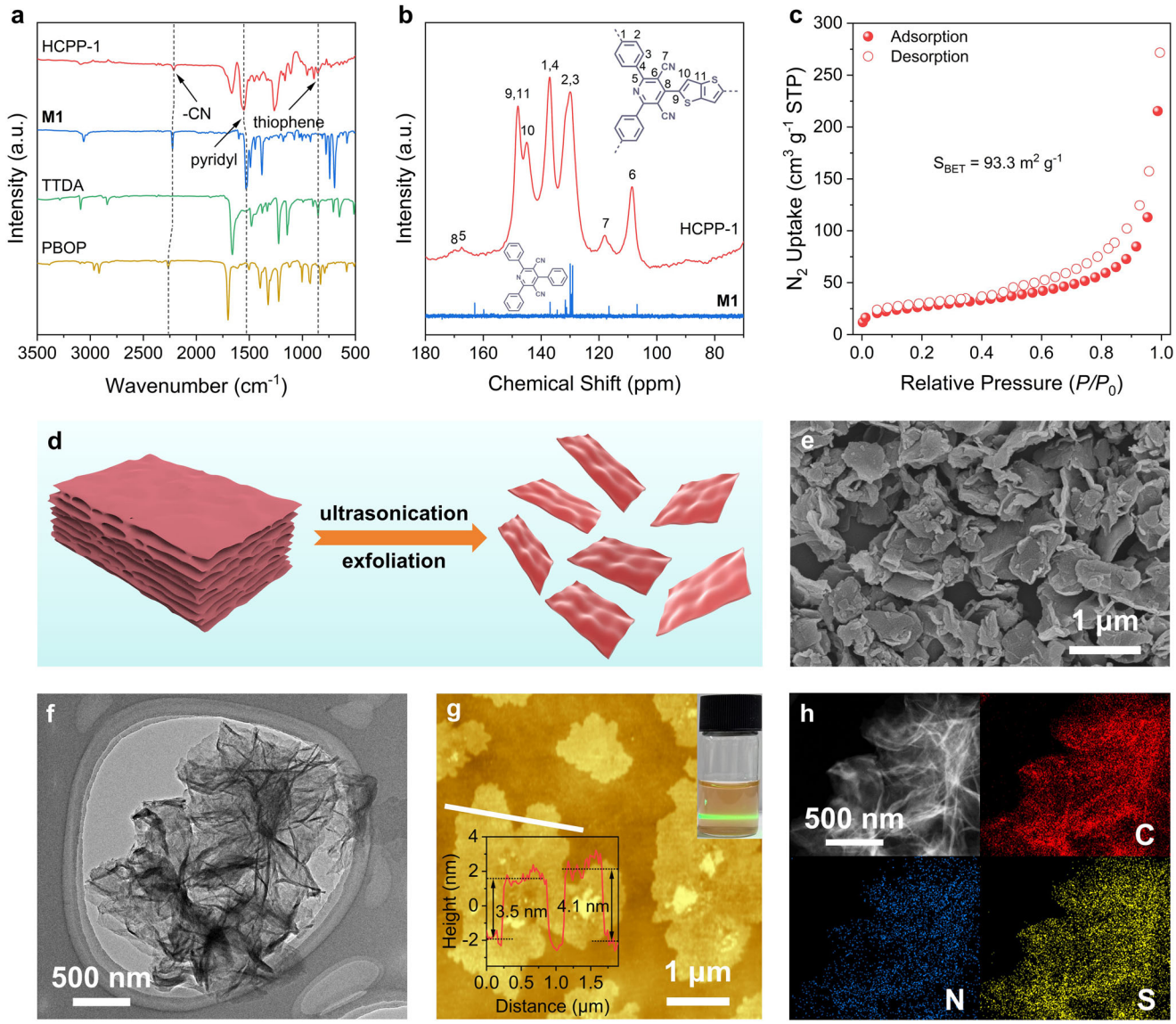


FIGURE 2 | (a) FT-IR spectra of HCPP-1, corresponding precursors TTDA and PBOP, and the model compound **M1**. (b) Solid-state ^{13}C CP/MAS NMR spectrum of HCPP-1 and liquid-state ^{13}C NMR spectrum of **M1** (Insets show their chemical structures). (c) N_2 sorption isotherms of HCPP-1 measured at 77 K. (d) Schematic illustration for the preparation of the exfoliated HCPP-1 nanosheets. (e) SEM image of HCPP-1. (f) TEM image, (g) AFM image (Insets show the height profile along the marked white line and the Tyndall effect of the sample's aqueous dispersion, respectively), and (h) HAADF-STEM elemental distribution of the C, N, and S elements of HCPP-1 nanosheets.

solid-state ^{13}C CP/MAS NMR spectrum of HCPP-1 and the liquid-state ^{13}C NMR spectrum of **M1** (Figure 2b) reveals matching signals for the corresponding carbon atoms. The peak at ~118 ppm is attributed to the carbon atom in the cyano group, while signals at ~109, 167, and 170 ppm originate from the pyridine ring carbons [46], collectively corroborating the formation of the proposed linkage, which, to the best of our knowledge, is reported here for the first time. Chemical shifts between 120 and 160 ppm are associated with carbon atoms in the phenyl and TT units. X-ray photoelectron spectroscopy (XPS) analysis was employed to investigate the chemical states of nitrogen atoms in HCPP-1. The high-resolution N 1s spectrum could be deconvoluted into two peaks at binding energies of 398.8 and 399.9 eV, corresponding to cyano N and pyridinic N, respectively (Figure S5) [46]. Powder x-ray diffraction (PXRD) analysis indicated that HCPP-1 is amorphous (Figure S6). The porosity was evaluated by N_2 adsorption–desorption measurements at 77 K. HCPP-1 displays a type IV isotherm with an H3 hysteresis loop, characteristic of a mesoporous structure (Figures 2c and S7). As determined by the Brunauer–Emmett–Teller method, the specific surface area of this material is 93.3 $m^2\ g^{-1}$. Although non-crystalline, this conjugated porous architecture exhibits a comparable surface area (e.g., 50–300 $m^2\ g^{-1}$ for typical amorphous conjugated microporous polymers, CMPs) [47], facilitating sufficient exposure of active sites to light and reactants, which is beneficial for both charge transfer and mass transport in photocatalytic processes. Thermogravimetric analysis (TGA) demonstrated that HCPP-1 is stable up to 365°C under an N_2 atmosphere (Figure S8), confirming its robust skeleton.

Two-dimensional (2D) nanosheets often exhibit enhanced photocatalytic activity compared to their bulk counterparts, owing

15213773, 2026, 42, Downloaded from https://onlinelibrary.wiley.com/doi/10.1002/anie.202527539 by Shengqian Ma - University Of North Texas Willis Library , Wiley Online Library on [21/10/2026]. See the Terms and Conditions (https://onlinelibrary.wiley.com/terms-and-conditions) on Wiley Online Library for rules of use; OA articles are governed by the applicable Creative Commons License

to reduced charge-carrier recombination and increased exposed surface area [48–50]. Given the weak π–π interlayer interactions in HCPP-1, the as-synthesized bulk material could be readily exfoliated into 2D polymer nanosheets (Figure 2d). Scanning electron microscopy (SEM) images reveal that the pristine HCPP-1 possesses a 2D sheet-like morphology with thicknesses of several tens of nanometers (Figures 2e and S9). Simple sonication in water exfoliated HCPP-1 into ultrathin, irregular nanosheets. Transmission electron microscopy (TEM) and atomic force microscopy (AFM) images of the exfoliated HCPP-1 nanosheets show a nearly transparent appearance with a thickness of approximately 4.0 nm and lateral dimensions of several micrometers (Figure 2f,g). The resulting nanosheets formed stable colloidal dispersions in water, as evidenced by a distinct Tyndall effect (inset, Figure 2g). Dynamic light scattering (DLS) measurements indicated a predominant colloidal size distribution centered around 349 nm (Figure S10). Furthermore, HCPP-1 exhibits hydrophilic character, with a water contact angle of 70.4° (Figure S11), which is conducive to the delivery of water and dissolved oxygen to the reactive sites within the π-conjugated skeleton. High-angle annular dark-field scanning TEM (HAADF-STEM) imaging and energy-dispersive x-ray (EDX) elemental mapping confirm the homogeneous distribution of C, N, and S elements throughout HCPP-1 nanosheets (Figure 2h), consistent with the XPS analysis (Figure S4).

The photophysical properties of HCPP-1 were investigated using UV–visible diffuse reflectance spectroscopy (UV–vis DRS), electron paramagnetic resonance (EPR), and photocurrent measurements. As shown in Figure 3a, HCPP-1 exhibits strong and broad absorption across the visible region, consistent with its observed color (Figure S12), underscoring its efficient light-harvesting capability. The optical bandgap (E_g) was estimated to be 1.98 eV from the corresponding Tauc plot (inset, Figure 3a). Notably, this intense visible-light absorption is retained even when HCPP-1 is dispersed in water. The valence band maximum (VBM) position was determined by valence band XPS (VB-XPS) (Figure S13). The VBM energy ($E_{VB,\,XPS}$) for HCPP-1 was measured to be 1.81 eV, corresponding to 1.57 V versus NHE ($E_{VB,\,NHE} = \varphi + E_{VB,\,XPS} - 4.44$, where the work function φ = 4.20 eV) [51]. Combined with the E_g value, the conduction band minimum (CBM) was calculated to be −0.41 V versus NHE. These results define the energy level diagram of HCPP-1 (Figure 3b), which thermodynamically supports its capability to drive the overall photosynthesis of H_2O_2 via dual-channel pathways. To evaluate charge separation efficiency, EPR spectra (g = 2.004) and photocurrent response were recorded under dark and visible-light illumination conditions (Figure 3c,d). Both the EPR signal intensity and photocurrent density increased markedly upon light irradiation, indicating efficient photogeneration and separation of charge carriers through electron transfer from the VB to the CB [52]. To sum up, HCPP-1 possesses comparable surface area, 2D ultrathin nanosheet morphology, hydrophilicity, good stability, extended π-conjugation, pronounced D–A effect (Figure S14), suitable energy band structure, and superior photo-responsiveness, suggesting its strong potential as an efficient photocatalyst for H_2O_2 production.

The photocatalytic performance of HCPP-1 for H_2O_2 production was evaluated using oxygen and water as reactants under xenon lamp irradiation. The concentration of generated H_2O_2 was quantified by iodometry (Figure S15). Remarkably, in the presence of benzyl alcohol as a sacrificial reagent, HCPP-1 achieved an ultrahigh H_2O_2 production rate of 19.06 μmol h^{-1} (corresponding to a gravimetric activity of 19.06 mmol g^{-1} h^{-1}) under visible-light irradiation ($\lambda > 420$ nm/100 mW cm^{-2}) (Figure S17), ranking it among the most active metal-free polymer photocatalysts reported to date and highlighting its exceptional potential [24, 42]. However, for practical applications requiring facile product separation and process sustainability, we focused on photocatalytic reactions in pure water without sacrificial agents. Initial optimization revealed that the optimal H_2O_2 production rate was achieved at a low catalyst concentration of 33 μg mL^{-1}, beyond which the yield decreased with increasing concentration, likely due to light-shielding effects impairing photon absorption (Figure S18). Control experiments confirmed that H_2O_2 generation was negligible in the absence of either light or the HCPP-1 catalyst (Figure S19), underscoring its indispensable role. Notably, as depicted in Figure 4a,b, HCPP-1 enables sustained H_2O_2 generation in O_2-saturated pure water under visible light, with an outstanding production rate of 5.23 μmol h^{-1} (5230 μmol g^{-1} h^{-1}), surpassing most previously reported photocatalysts under comparable conditions. A comparison with representative materials is summarized in Figure 4c and Table S2. When the reaction atmosphere was switched from pure O_2 to ambient air (21% O_2), the H_2O_2 production rate decreased to 3.69 μmol h^{-1} (3690 μmol g^{-1} h^{-1}), retaining over 70% of the original efficiency, a performance that remains highly competitive (Figure 4a,b and Table S3). To further probe the light-harvesting and conversion capability of HCPP-1, its apparent quantum yield (AQY) was measured under monochromatic light irradiation. The action spectrum for H_2O_2 production closely aligns with the optical absorption profile of HCPP-1 (Figure 4d), confirming a photo-driven catalytic mechanism. The AQY reaches a maximum of 6.35% at 450 nm and remains as high as 2.14% even at a long wavelength of 650 nm (Table S2), indicating promising potential for broadband solar-driven H_2O_2 synthesis. The reusability of HCPP-1 was assessed over five consecutive 1-hour photocatalytic cycles in pure water under an O_2 atmosphere and visible-light illumination. As shown in Figure 4e, only a marginal decline in H_2O_2 yield was observed. Post-reaction characterization by FT-IR, XPS, SEM, and TEM revealed no significant alterations in the chemical structure or morphology of the catalyst (Figures 4f and S20), collectively confirming its exceptional structural stability. This robustness was further corroborated by a 20 h long-term photocatalytic test (Figure S21). These findings demonstrate that polymers derived from the Hantzsch-type reaction hold considerable promise for efficient and stable H_2O_2 photosynthesis.

The mechanism of photocatalytic H_2O_2 generation was investigated through control experiments, isotope labeling, in situ characterizations, and density functional theory (DFT) calculations. As shown in Figure 5a, replacing O_2 with argon (Ar) led to a sharp decrease in H_2O_2 production; however, a residual rate of 0.62 μmol h^{-1} was still observed, suggesting that the ORR pathway dominates, while the WOR pathway also contributes. To identify the specific WOR pathway, tert-butyl alcohol (TBA), a hydroxyl radical ($^{\bullet}OH$) scavenger, was introduced. The absence of any noticeable change in H_2O_2 yield (Figure 5a) rules out an $^{\bullet}OH$-mediated WOR process, a result consistent with energy diagram predictions and EPR analysis (Figure S22). Furthermore, no H_2O_2 was detected when $AgNO_3$ (an electron scavenger) was present, precluding a one-step direct WOR process. This implies

15213773, 2026, 42, Downloaded from https://onlinelibrary.wiley.com/doi/10.1002/anie.a237539 by Shengqian Ma - University Of North Texas Willis Library , Wiley Online Library on [21/10/2026]. See the Terms and Conditions (https://onlinelibrary.wiley.com/terms-and-conditions) on Wiley Online Library for rules of use; OA articles are governed by the applicable Creative Commons License

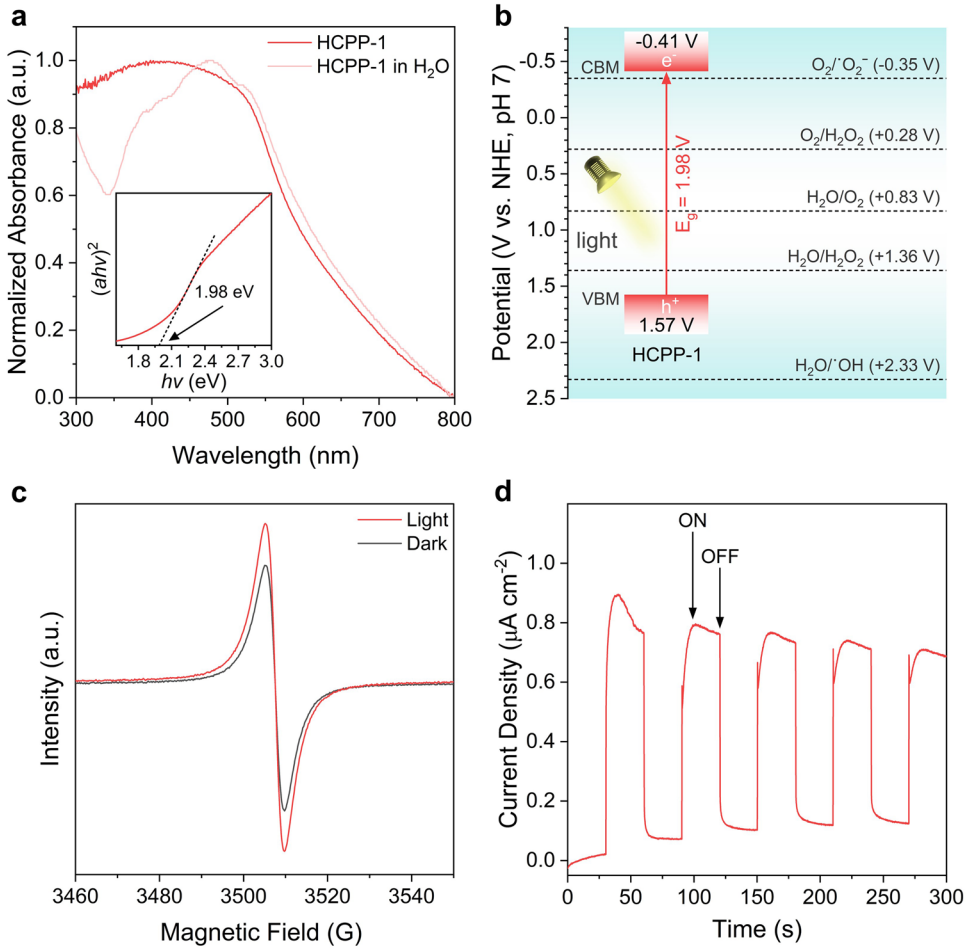


FIGURE 3 | (a) UV–vis DRS spectrum of HCPP-1 and its corresponding aqueous spectrum (Inset shows the Tauc plot). (b) Energy band diagram of HCPP-1. (c) EPR spectra and (d) Transient photocurrents of HCPP-1 in the dark and after illumination ($\lambda > 420$ nm, 300 W Xe lamp).

that a 4e⁻ WOR pathway likely operates in the current system. The addition of *p*-benzoquinone (pBQ), a superoxide radical ($^{\bullet}O_2^-$) trapping agent, completely suppressed H_2O_2 production, demonstrating the critical role of $^{\bullet}O_2^-$. Its formation was directly confirmed by EPR spectroscopy using 5,5-dimethyl-1-pyrroline N-oxide (DMPO) as a spin trap, where characteristic signals for DMPO-$^{\bullet}O_2^-$ adducts were observed under visible-light irradiation (Figure 5b). The absence of an EPR signal characteristic of singlet oxygen ($^1O_2$) excludes the likelihood of $^1O_2$ involvement (Figure S23). These results reveal that H_2O_2 generation proceeds predominantly via a $^{\bullet}O_2^-$-mediated two-step 2e⁻ ORR pathway. Isotope labeling experiments were conducted to further verify the reaction pathways. When the reaction was conducted under atmospheres of $^{16}O_2$ and $^{18}O_2$, respectively, the resulting H_2O_2 was decomposed using MnO_2, and the evolved oxygen was analyzed. The mass spectrometry data revealed a distinct signal corresponding exclusively to $^{16}O_2$ in the former case, and a high ratio of $^{18}O_2$ to $^{16}O_2$ in the latter (Figures S24a and 5c). These findings indicate that H_2O_2 is dominantly generated via the reduction of molecular oxygen. When the reaction was carried out in Ar-saturated $H_2{}^{18}O$ containing $AgNO_3$, $^{18}O_2$ was directly detected by gas chromatography-mass spectrometry (GC-MS), which, together with the control experiment (Figure S24b), confirms the occurrence of a 4e⁻ WOR process. Additionally, the evolution of a stoichiometric amount of O_2 in the water oxidation half-reaction strongly substantiates the claim of the 4e⁻ WOR pathway (Figure S25). Moreover, simultaneous labeling of both O_2 and H_2O reactants yielded a significantly higher $^{18}O_2/^{16}O_2$ ratio compared to the case with only O_2 labeling (Figure S26), revealing that O_2 produced via WOR is subsequently consumed in the ORR to generate additional H_2O_2 [40, 50].

In situ diffuse reflectance infrared Fourier transform spectroscopy (DRIFTS) of HCPP-1 under an oxygen and steam atmosphere provided further evidence for reactive intermediates and the photocatalytic pathway (Figure 5d–f). A characteristic signal at 2877 cm^{-1}, assigned to the O–H bending mode of H_2O_2, appeared and intensified with reaction time (Figure 5d), offering direct evidence for photocatalytic H_2O_2 production. Interestingly, the intensities of peaks corresponding to C=C stretching vibrations (1488 and 1612 cm^{-1}) of the benzene ring adjacent to the linkage also varied with prolonged irradiation (Figure 5e), suggesting its involvement as an active site [40, 53]. Furthermore, peaks associated with the endoperoxide *OOH (1209 cm^{-1}), $^{\bullet}O_2^-$ (1138 cm^{-1}), and O–O (869 cm^{-1}) species increased in intensity (Figure 5f), indicating O_2 adsorption and the occurrence of the two-step 2e⁻ ORR pathway via superoxide radical anion intermediates [40, 54, 55]. Concurrently, signals attributed to C–OH (1086 cm^{-1}) and C–O (1396 cm^{-1}) species proved the

15213773, 2026, 42, Downloaded from https://onlinelibrary.wiley.com/doi/10.1002/anie.e237539 by Shengqian Ma - University Of North Texas Willis Library , Wiley Online Library on [21/10/2026]. See the Terms and Conditions (https://onlinelibrary.wiley.com/terms-and-conditions) on Wiley Online Library for rules of use; OA articles are governed by the applicable Creative Commons License

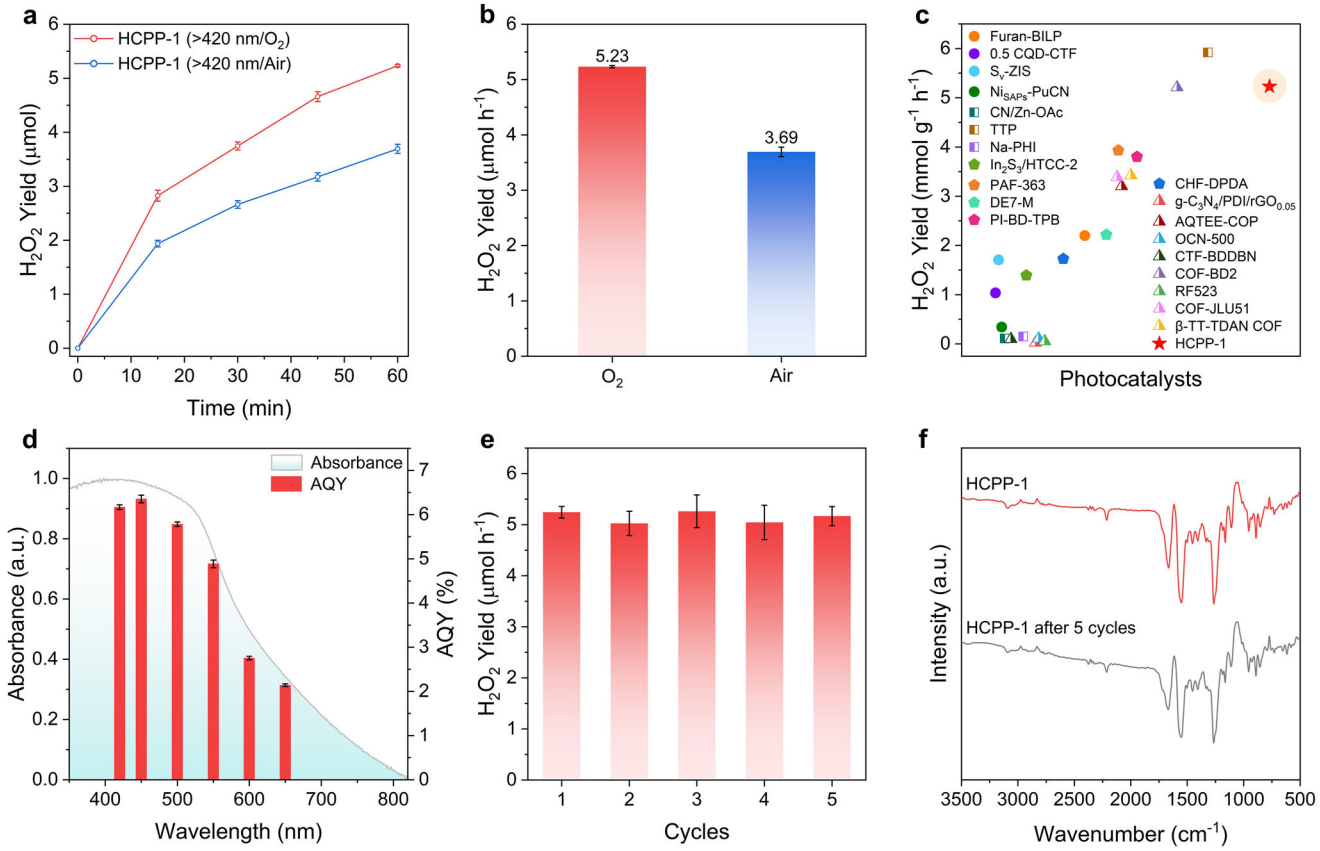


FIGURE 4 | (a) Time courses of photocatalytic H_2O_2 production and (b) H_2O_2 production rates for HCPP-1 in O_2- and air-saturated pure water without sacrificial agents under visible-light irradiation ($\lambda > 420$ nm/100 mW cm^{-2}). (c) Comparison of the H_2O_2 productivity for HCPP-1 with the reported representative photocatalysts under comparable conditions, with summarized data provided in Table S2. (d) UV–vis DRS spectrum and AQY of H_2O_2 production for HCPP-1. (e) Photocatalytic cycling test of HCPP-1 (Conditions: pure water, O_2, and $\lambda > 420$ nm/100 mW cm^{-2}). (f) FT-IR spectra of HCPP-1 undergoing recycling experiments. Error bars are the standard deviations of three independent experiments.

existence of the 4e$^-$ WOR process (Figure 5f) [19, 54]. Collectively, these results unequivocally demonstrate that HCPP-1 enables synergistic catalysis involving the indirect 2e$^-$ ORR and 4e$^-$ WOR pathways. This dual-channel mechanism not only enhances the utilization efficiency of photogenerated charge carriers but also mitigates hole accumulation-induced catalyst degradation [56], ultimately achieving efficient non-sacrificial H_2O_2 production.

DFT calculations were performed to identify the photocatalytically active centers in HCPP-1 and elucidate the underlying reaction mechanism. Considering that HCPP-1 is amorphous rather than crystalline, a simplified structural fragment, denoted as HCPP-1f, comprising the linkage connected to the TT and phenyl groups (inset, Figure 5h), was used for modeling. The spatial distribution of the frontier molecular orbitals was analyzed (Figure 5g). The highest occupied molecular orbital (HOMO) is primarily localized on the electron-donating TT moiety, whereas the lowest unoccupied molecular orbital (LUMO) is concentrated on the electron-accepting linkage and adjacent benzene rings. This assignment is corroborated by the electrostatic surface potential (ESP) map of HCPP-1f, which shows a clear separation of positive and negative charges (Figure S27). The distinct spatial separation facilitates light-induced electron transfer from the TT donor to the acceptor units, promoting efficient charge separation, a critical factor for high photocatalytic performance [51, 57]. Consequently, the TT moieties are identified as potential oxidation sites, while the linkage and benzene rings serve as reduction sites.

Guided by experimental evidence for the dual-channel H_2O_2 production pathway, we computed the Gibbs free energy (ΔG) profiles for both the ORR and WOR processes on various potential active sites [58, 59]. In situ DRIFTS indicated the benzene ring's involvement in reaction processes. Accordingly, ΔG analyses for *OOH intermediate formation, a key ORR step, were conducted on the benzene, TT, cyano, and pyridine moieties. As illustrated in Figure 5h, the benzene ring exhibits the most favorable ΔG for *OOH formation, implying that it acts as the primary ORR active site, in good agreement with DRIFTS and frontier orbital results. For the 4e$^-$ WOR pathway, which involves H_2O deprotonation to form *OH, followed by the formation of *O, *O*OH, and *OO* intermediates [40, 50, 59], DFT calculations identified the TT moiety as the most active site (Figures 5i and S28). The TT site possesses the lowest energy barrier for the rate-determining step of *OO* formation ($\Delta G = 1.89$ eV), significantly lower than those for *OH formation on the benzene (4.65 eV), cyano (3.89 eV), and pyridine (2.10 eV) moieties. These findings also indicate that the redox centers on HCPP-1 are spatially separated during photocatalysis, which is expected to suppress charge recombination and thereby facilitate H_2O_2 production

15213773, 2026, 42, Downloaded from https://onlinelibrary.wiley.com/doi/10.1002/anie.e237539 by Shengqian Ma - University Of North Texas Willis Library , Wiley Online Library on [21/10/2026]. See the Terms and Conditions (https://onlinelibrary.wiley.com/terms-and-conditions) on Wiley Online Library for rules of use; OA articles are governed by the applicable Creative Commons License

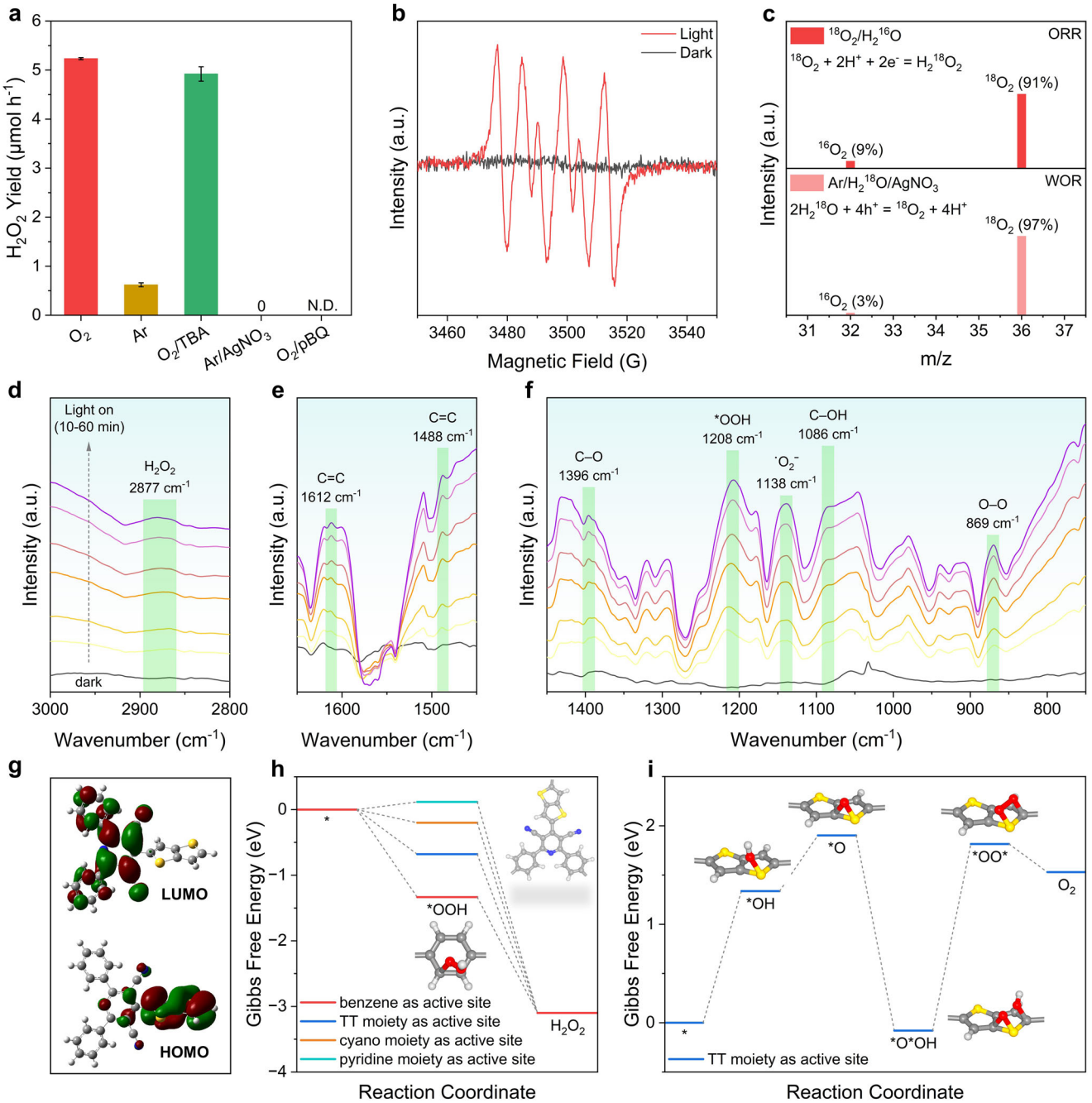


FIGURE 5 | (a) Photocatalytic H_2O_2 production of HCPP-1 under different conditions (TBA as the hydroxyl radical trapping agent, $AgNO_3$ as the electron scavenger, and pBQ as the superoxide radical trapping agent). (b) EPR spectra of HCPP-1 in the dark and under visible-light irradiation using DMPO as the spin-trapping reagent. (c) Isotopic experiments for HCPP-1 operating in the presence of $^{18}O_2/H_2{}^{16}O$ (upper part) and $Ar/H_2{}^{18}O/AgNO_3$ (bottom part) to explore ORR and WOR half-reactions, respectively. (d–f) In situ DRIFTS spectra of HCPP-1 recorded at different photoirradiation times under O_2 and steam environments, from 3000–2800 cm^{-1} (d), 1650–1450 cm^{-1} (e), and 1450–750 cm^{-1} (f). (g) Calculated HOMO and LUMO distributions of the simplified structural fragment HCPP-1f. (h) Gibbs free energy diagram of the ORR pathway toward H_2O_2 production on different active sites in HCPP-1 (Insets show the optimized configuration of the benzene active site and the model structure, respectively). (i) Gibbs free energy diagram of the WOR pathway on the TT moiety in HCPP-1 (Insets show the optimized configurations for each step). Error bars are the standard deviations of three independent experiments.

[18, 19]. The overall photocatalytic reaction mechanism for HCPP-1, integrating experimental and theoretical evidence, is summarized in Figure S29. It can be described as follows: O_2 is adsorbed and sequentially reduced by two proton-electron pairs at the benzene ring sites, forming an *OOH intermediate and then H_2O_2. Concurrently, photoinduced holes oxidize H_2O at the TT sites, generating O_2 and protons, which in turn serve as reactants for the $2e^-$ ORR.

Encouraged by the efficient photocatalytic H_2O_2 production of HCPP-1, we investigated its performance under ambient conditions mimicking natural environments (seawater, air, and

15213773, 2026, 42, Downloaded from https://onlinelibrary.wiley.com/doi/10.1002/anie.a237539 by Shengqian Ma - University Of North Texas Willis Library , Wiley Online Library on [21/10/2026]. See the Terms and Conditions (https://onlinelibrary.wiley.com/terms-and-conditions) on Wiley Online Library for rules of use; OA articles are governed by the applicable Creative Commons License

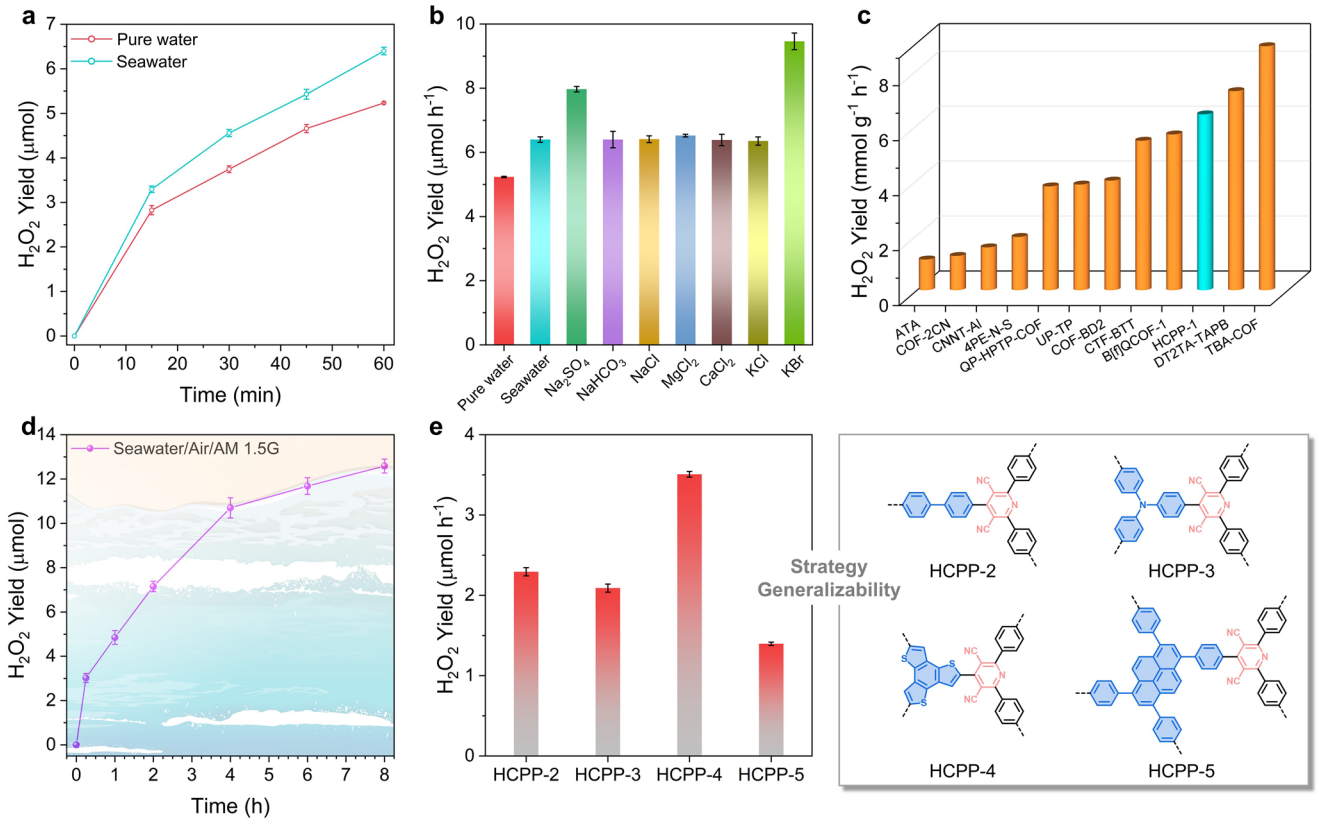


FIGURE 6 | (a) Photocatalytic H_2O_2 production performance of HCPP-1 in O_2-saturated pure water and real seawater (from the Bohai Sea, China) without sacrificial agents under visible-light irradiation (λ > 420 nm/100 mW cm^{-2}). (b) The effect of salts in real seawater on the H_2O_2 production rate of HCPP-1. (c) The photoactivity of HCPP-1 in comparison with reported photocatalysts (Conditions: seawater, O_2, visible-light irradiation, and free of sacrificial agents), with summarized data provided in Table S4. (d) The photogenerated H_2O_2 concentration of HCPP-1 with prolonged irradiation time over 8 h (Conditions: seawater, air, free of sacrificial agents, and simulated solar irradiation/100 mW cm^{-2}). (e) Generalizable structure diagram and photocatalytic H_2O_2 production efficiency of HCPP-2 to HCPP-5 with varied D–A architectures to assess the general applicability of this developed synthetic strategy. Error bars are the standard deviations of three independent experiments.

sunlight) to evaluate its potential for practical H_2O_2 synthesis. We first examined the effect of pH (3–11) on H_2O_2 production. Notably, HCPP-1 maintained appreciable production rates in alkaline media (Figure S30), an advantage for photocatalysis in seawater. Subsequently, photocatalytic efficiency was assessed in O_2-saturated natural seawater (from the Bohai Sea, China) under visible-light irradiation. Impressively, HCPP-1 achieved an H_2O_2 production rate of 6.40 μmol h^{-1}, surpassing its performance in pure water (Figure 6a). To understand this enhancement, photocatalytic experiments were conducted in simulated seawater containing various salts (Na_2SO_4, $NaHCO_3$, NaCl, $MgCl_2$, $CaCl_2$, KCl, and KBr) at concentrations identical to natural seawater. The introduction of these inorganic salts significantly boosted H_2O_2 production, with KBr exhibiting the most pronounced promotion effect (Figure 6b). This result can be attributed to K^+-induced surface ionization and Br^--mediated hole extraction ($E_{VB,\ NHE}$ = 1.57 V for HCPP-1 vs. $E_{redox,\ NHE}$ = 1.07 V for Br_2/Br^-), thereby suppressing electron-hole recombination [43, 60, 61], which is supported by the obvious fluorescence quenching observed in photoluminescence (PL) spectra upon the addition of KBr (Figure S31). The remarkable H_2O_2 production efficiency of 6400 μmol g^{-1} h^{-1} in seawater positions HCPP-1 as highly competitive among state-of-the-art photocatalysts (Figure 6c and Table S4). Furthermore, a fully environmentally relevant system (seawater, air, free of sacrificial agents, and simulated AM 1.5G solar irradiation/100 mW cm^{-2}) was employed to evaluate long-term H_2O_2 production (Figure 6d). Over an 8 h period, HCPP-1 achieved a notable production rate of 4.85 μmol h^{-1} (4850 μmol g^{-1} h^{-1}) within the first hour, outperforming nearly all the reported photocatalysts (Table S5). H_2O_2 accumulation continued over the 8 h irradiation, delivering a yield of 12.59 mmol g^{-1}, albeit at gradually diminishing rates, which is likely due to H_2O_2 self-decomposition, a common phenomenon in photocatalytic systems [8, 62]. Importantly, HCPP-1 retained considerable photocatalytic activity after recovery and reuse in a fresh reaction, demonstrating its practical robustness.

To assess the generalizability of the Hantzsch reaction-based strategy in constructing CPPs for solar-to-chemical conversion, we synthesized four additional D–A type HCPPs (HCPP-2 to HCPP-5) using biphenyl, triarylamine, trithiophene, and pyrene building units, respectively (Figure 6e and Scheme S4). These monomers were selected to encompass a range of electronic properties and geometric configurations. The chemical structures, morphologies, optical properties, and energy levels of these HCPPs were systematically characterized by FT-IR, SEM, UV–vis DRS, and XPS (Figures S32–S36). Note that owing to their distinct electronic and energy band structures, the specific reaction

15213773, 2026, 42, Downloaded from https://onlinelibrary.wiley.com/doi/10.1002/anie.4237539 by Shengqian Ma - University Of North Texas Willis Library , Wiley Online Library on [21/10/2026]. See the Terms and Conditions (https://onlinelibrary.wiley.com/terms-and-conditions) on Wiley Online Library for rules of use; OA articles are governed by the applicable Creative Commons License

mechanisms for H_2O_2 generation in these HCPPs may differ from those of HCPP-1. Under light irradiation, all polymers demonstrated promising photocatalytic H_2O_2 production performance. These results validate the general applicability of our synthetic strategy and open a novel route for constructing high-efficiency CPP photocatalysts.

3 | Conclusion

In summary, we have established a versatile synthetic platform based on a Hantzsch-type MCR approach to construct a new family of CPPs. By strategically integrating pyridine-3,5-dicarbonitrile units as dual-function motifs that serve simultaneously as robust structural linkages and electron-accepting centers, we engineered a series of D–A pyridine-3,5-dicarbonitrile-linked HCPPs capable of efficient, sacrificial-agent-free photocatalytic H_2O_2 production. Exemplified by the thieno[3,2-b]thiophene-based HCPP-1, comprehensive studies reveal that its ultrathin exfoliated morphology, hydrophilicity, broad visible-light absorption, strong D–A interactions, and spatially segregated redox sites synergistically enable exceptional photocatalytic activity, delivering a high H_2O_2 production rate of 5230 μmol g^{-1} h^{-1} from H_2O and O_2 under visible light, with an AQY of 2.14% at 650 nm. Mechanistic investigations uncover a dual-channel pathway involving indirect $2e^-$ ORR at benzene rings and $4e^-$ WOR at thieno[3,2-b]thiophene moieties. Remarkably, HCPP-1 retains outstanding performance (4850 μmol g^{-1} h^{-1}) under environmentally relevant conditions (natural seawater, ambient air, and simulated sunlight), placing it among the top-performing photocatalysts. This work not only expands the synthetic toolbox for functional conjugated polymers but also offers a new avenue for rationally designing next-generation photocatalysts tailored for practical, solar-driven H_2O_2 synthesis.

Author Contributions

Changgui Lv: methodology, data curation, investigation, validation, formal analysis, writing – original draft. **Jingmin Ge:** data curation, investigation. **Xikai Chen:** data curation, investigation. **Jinyu Liu:** data curation, investigation. **Yanming Zhao:** conceptualization, funding acquisition, supervision, resources, project administration, writing – original draft. **Abdullah M. Al-enizi:** resources, writing – review and editing, funding acquisition. **Ayman Nafady:** resources, writing – review and editing, funding acquisition. **Shengqian Ma:** conceptualization, writing – review and editing, resources, funding acquisition.

Acknowledgments

The authors acknowledge the National Natural Science Foundation of China (No. 22201258) and the China Postdoctoral Science Foundation (Nos. 2023TQ0323 and 2024M752928) for financial support. Partial support from the Robert A Welch Foundation (B-0027) (SM) and the Ongoing Research Funding Program (ORF-2026-79), King Saud University, Riyadh, Saudi Arabia (AN) is also acknowledged.

Conflicts of Interest

The authors declare no conflicts of interest.

Data Availability Statement

The data that support the findings of this study are available from the corresponding author upon reasonable request.

References

1. K. P. Bryliakov, "Catalytic Asymmetric Oxygenations with the Environmentally Benign Oxidants H_2O_2 and O_2," *Chemical Reviews* 117 (2017): 11406–11459, https://doi.org/10.1021/acs.chemrev.7b00167.

2. W. Fan, B. Zhang, X. Wang, et al., "Efficient Hydrogen Peroxide Synthesis by Metal-Free Polyterthiophene via Photoelectrocatalytic Dioxygen Reduction," *Energy & Environmental Science* 13 (2020): 238–245, https://doi.org/10.1039/C9EE02247C.

3. C. Xia, Y. Xia, P. Zhu, L. Fan, and H. Wang, "Direct Electrosynthesis of Pure Aqueous H_2O_2 Solutions up to 20% by Weight Using a Solid Electrolyte," *Science* 366 (2019): 226–231, https://doi.org/10.1126/science.aay1844.

4. D. Kim, K. K. Sakimoto, D. Hong, and P. Yang, "Artificial Photosynthesis for Sustainable Fuel and Chemical Production," *Angewandte Chemie International Edition* 54 (2015): 3259–3266, https://doi.org/10.1002/anie.201409116.

5. S. Yang, A. Verdaguer-Casadevall, L. Arnarson, et al., "Toward the Decentralized Electrochemical Production of H_2O_2: A Focus on the Catalysis," *ACS Catalysis* 8 (2018): 4064–4081, https://doi.org/10.1021/acscatal.8b00217.

6. J. M. Campos-Martin, G. Blanco-Brieva, and J. L. G. Fierro, "Hydrogen Peroxide Synthesis: An Outlook Beyond the Anthraquinone Process," *Angewandte Chemie International Edition* 45 (2006): 6962–6984, https://doi.org/10.1002/anie.200503779.

7. X. Xu, Y. Sui, W. Chen, et al., "The Photocatalytic H_2O_2 Production by Metal-Free Photocatalysts Under Visible-Light Irradiation," *Applied Catalysis B* 341 (2024): 123271, https://doi.org/10.1016/j.apcatb.2023.123271.

8. Y. Zhang, C. Pan, G. Bian, et al., "H_2O_2 Generation From O_2 and H_2O on a Near-Infrared Absorbing Porphyrin Supramolecular Photocatalyst," *Nature Energy* 8 (2023): 361–371.

9. H. Hou, X. Zeng, and X. Zhang, "Production of Hydrogen Peroxide by Photocatalytic Processes," *Angewandte Chemie International Edition* 59 (2020): 17356–17376, https://doi.org/10.1002/anie.201911609.

10. Z. Teng, Q. Zhang, H. Yang, et al., "Atomically Dispersed Antimony on Carbon Nitride for the Artificial Photosynthesis of Hydrogen Peroxide," *Nature Catalysis* 4 (2021): 374–384, https://doi.org/10.1038/s41929-021-00605-1.

11. Z. Teng, H. Yang, Q. Zhang, et al., "Atomically Dispersed Low-Valent Au Boosts Photocatalytic Hydroxyl Radical Production," *Nature Chemistry* 16 (2024): 1250–1260, https://doi.org/10.1038/s41557-024-01553-6.

12. Z. Zhang, Y. Hou, S. Zhu, et al., "Benzotrifuran-Based Covalent Organic Frameworks for Artificial Photosynthesis of H_2O_2 From H_2O, O_2, and Sunlight," *Angewandte Chemie International Edition* 64 (2025): e202505286.

13. H. Peng, H. Yang, J. Han, et al., "Defective $ZnIn_2S_4$ Nanosheets for Visible-Light and Sacrificial-AgentFree H_2O_2 Photosynthesis via O_2/H_2O Redox," *Journal of the American Chemical Society* 145 (2023): 27757–27766.

14. H. Tan, P. Zhou, M. Liu, et al., "Al–N_3 Bridge Site Enabling Interlayer Charge Transfer Boosts the Direct Photosynthesis of Hydrogen Peroxide From Water and Air," *Journal of the American Chemical Society* 146 (2024): 31950–31960, https://doi.org/10.1021/jacs.4c11471.

15. J.-Y. Yue, L.-P. Song, Y.-F. Fan, et al., "Thiophene-Containing Covalent Organic Frameworks for Overall Photocatalytic H_2O_2 Synthesis in Water and Seawater," *Angewandte Chemie International Edition* 62 (2023): e202309624, https://doi.org/10.1002/anie.202309624.

16. C. Wu, Z. Teng, C. Yang, et al., "Polarization Engineering of Covalent Triazine Frameworks for Highly Efficient Photosynthesis of Hydrogen Peroxide From Molecular Oxygen and Water," *Advanced Materials* 34 (2022): 2110266, https://doi.org/10.1002/adma.202110266.

17. T. Yang, D. Zhang, A. Kong, et al., "Robust Covalent Organic Framework Photocatalysts for H_2O_2 Production: Linkage Position Matters,"

15213773, 2026, 42, Downloaded from https://onlinelibrary.wiley.com/doi/10.1002/anie.e237539 by Shengqian Ma - University Of North Texas Willis Library , Wiley Online Library on [21/10/2026]. See the Terms and Conditions (https://onlinelibrary.wiley.com/terms-and-conditions) on Wiley Online Library for rules of use; OA articles are governed by the applicable Creative Commons License

Angewandte Chemie International Edition 63 (2024): e202404077, https://doi.org/10.1002/anie.202404077.

18. H. Cheng, H. Lv, J. Cheng, L. Wang, X. Wu, and H. Xu, "Rational Design of Covalent Heptazine Frameworks With Spatially Separated Redox Centers for High-Efficiency Photocatalytic Hydrogen Peroxide Production," *Advanced Materials* 34 (2021): 2107480, https://doi.org/10.1002/adma.202107480.

19. C. Qin, X. Wu, L. Tang, et al., "Dual Donor-Acceptor Covalent Organic Frameworks for Hydrogen Peroxide Photosynthesis," *Nature Communications* 14 (2023): 5238, https://doi.org/10.1038/s41467-023-40991-7.

20. J.-R. Huang, H.-Y. Chen, H.-L. Zhu, P.-Q. Liao, and X.-M. Chen, "Ni–Zn Dual-Atom Sites Enable Synergistic Parallel Pathways for Efficient Photosynthesis of H_2O_2 With Long-Term Stability," *Journal of the American Chemical Society* 147 (2025): 37167–37175, https://doi.org/10.1021/jacs.5c09202.

21. J. Byun and K. A. I. Zhang, "Designing Conjugated Porous Polymers for Visible Light-Driven Photocatalytic Chemical Transformations," *Mater Horiz* 7 (2020): 15–31, https://doi.org/10.1039/C9MH01071H.

22. Z. Yong and T. Ma, "Solar-to-H_2O_2 Catalyzed by Covalent Organic Frameworks," *Angewandte Chemie International Edition* 62 (2023): e202308980.

23. J. Tang, Z. Jiang, Z. Gao, et al., "Hydroxyl Radical Mediated Heterogeneous Photocatalytic Baeyer–Villiger Oxidation Over Covalent Triazine/Heptazine-Based Frameworks," *Angewandte Chemie International Edition* 64 (2025): e202416879, https://doi.org/10.1002/anie.202416879.

24. L. Cao, C. Wang, H. Wang, et al., "Rationally Designed Cyclooctatetrathiophene-Based Porous Aromatic Frameworks (COTh-PAFs) for Efficient Photocatalytic Hydrogen Peroxide Production," *Angewandte Chemie International Edition* 63 (2024): e202402095, https://doi.org/10.1002/anie.202402095.

25. H. Yan, Y. Huang, M. Shen, J. Xu, Y. X. Ye, and G. Ouyang, "Enhancing Solar-to-Hydrogen Peroxide Conversion Efficiency by Promoting the Two-Electron Water Oxidation Pathway via Modulating the Main Electron Transition Orbital," *Angewandte Chemie International Edition* 137 (2025): e202425054, https://doi.org/10.1002/ange.202425054.

26. G. Li, T. Qiu, Q. Wu, et al., "Pyrene-Alkyne-Based Conjugated Porous Polymers With Skeleton Distortion-Mediated $\cdot O_2^-$ and $^1O_2$ Generation for High-Selectivity Organic Photosynthesis," *Angewandte Chemie International Edition* 63 (2024): e202405396, https://doi.org/10.1002/anie.202405396.

27. A. Dömling, W. Wang, and K. Wang, "Chemistry and Biology of Multicomponent Reactions," *Chemical Reviews* 112 (2012): 3083–3135.

28. S. Brauch, S. S. van Berkel, and B. Westermann, "Higher-Order Multicomponent Reactions: Beyond Four Reactants," *Chemical Society Reviews* 42 (2013): 4948, https://doi.org/10.1039/c3cs35505e.

29. L. Reguera and D. G. Rivera, "Multicomponent Reaction Toolbox for Peptide Macrocyclization and Stapling," *Chemical Reviews* 119 (2019): 9836–9860, https://doi.org/10.1021/acs.chemrev.8b00744.

30. R. Kakuchi, "Multicomponent Reactions in Polymer Synthesis," *Angewandte Chemie International Edition* 53 (2014): 46–48, https://doi.org/10.1002/anie.201305538.

31. Q. Guan, L.-L. Zhou, and Y.-B. Dong, "Construction of Covalent Organic Frameworks via Multicomponent Reactions," *Journal of the American Chemical Society* 145 (2023): 1475–1496, https://doi.org/10.1021/jacs.2c11071.

32. A. Hantzsch, "Condensationsprodukte aus Aldehydammoniak und Ketonartigen Verbindungen," *Berichte Der Deutschen Chemischen Gesellschaft* 14 (1881): 1637–1638, https://doi.org/10.1002/cber.18810140214.

33. O. Quinonero, M. Jean, N. Vanthuyne, et al., "Combining Organocatalysis With Central-to-Axial Chirality Conversion: Atroposelective Hantzsch-Type Synthesis of 4-Arylpyridines," *Angewandte Chemie International Edition* 55 (2016): 1401–1405, https://doi.org/10.1002/anie.201509967.

34. H. Wu, Z. Wang, and L. Tao, "The Hantzsch Reaction in Polymer Chemistry: Synthesis and Tentative Application," *Polymer Chemistry* 8 (2017): 7290–7296, https://doi.org/10.1039/C7PY01718A.

35. X. Li, Y. Che, L. Chen, et al., "Sequential Closed-Loop Bayesian Optimization as a Guide for Organic Molecular Metallophotocatalyst Formulation Discovery," *Nature Chemistry* 16 (2024): 1286–1294, https://doi.org/10.1038/s41557-024-01546-5.

36. D. M. Stout and A. I. Meyers, "Recent Advances in the Chemistry of Dihydropyridines," *Chemical Reviews* 82 (1982): 223–243, https://doi.org/10.1021/cr00048a004.

37. G. Liu, Y. Zeng, T. Lv, et al., "High-Throughput Preparation of Radioprotective Polymers via Hantzsch's Reaction for in Vivo X-Ray Damage Determination," *Nature Communications* 11 (2020): 6214, https://doi.org/10.1038/s41467-020-20027-0.

38. P.-Z. Wang, J.-R. Chen, W.-J. Xiao, and H. Esters, "Hantzsch Esters: An Emerging Versatile Class of Reagents in Photoredox Catalyzed Organic Synthesis," *Organic & Biomolecular Chemistry* 17 (2019): 6936–6951, https://doi.org/10.1039/C9OB01289C.

39. C. Allais, J.-M. Grassot, J. Rodriguez, and T. Constantieux, "Metal-Free Multicomponent Syntheses of Pyridines," *Chemical Reviews* 114 (2014): 10829–10868, https://doi.org/10.1021/cr500099b.

40. R. Liu, Y. Chen, H. Yu, et al., "Linkage-Engineered Donor–Acceptor Covalent Organic Frameworks for Optimal Photosynthesis of Hydrogen Peroxide from Water and Air," *Nature Catalysis* 7 (2024): 195–206, https://doi.org/10.1038/s41929-023-01102-3.

41. J. Cheng, W. Wang, J. Zhang, et al., "Molecularly Tunable Heterostructured Co-Polymers Containing Electron-Deficient and -Rich Moieties for Visible-Light and Sacrificial-Agent-Free H_2O_2 Photosynthesis," *Angewandte Chemie International Edition* 136 (2024): e202406310, https://doi.org/10.1002/ange.202406310.

42. K.-H. Xie, G.-B. Wang, F. Huang, et al., "Multicomponent One-Pot Construction of Benzo[f]Quinoline-Linked Covalent Organic Frameworks for H_2O_2 Photosynthesis," *Nature Communications* 16 (2025): 3493, https://doi.org/10.1038/s41467-025-58839-7.

43. A. Gopakumar, P. Ren, J. Chen, et al., "Lignin-Supported Heterogeneous Photocatalyst for the Direct Generation of H_2O_2 from Seawater," *Journal of the American Chemical Society* 144 (2022): 2603–2613, https://doi.org/10.1021/jacs.1c10786.

44. Z. Luo, X. Chen, Y. Hu, et al., "Side-Chain Molecular Engineering of Triazole-Based Donor-Acceptor Polymeric Photocatalysts With Strong Electron Push-Pull Interactions," *Angewandte Chemie International Edition* 62 (2023): e202304875, https://doi.org/10.1002/anie.202304875.

45. W. Zhang, M. Yu, T. Liu, et al., "Accelerated Discovery of Molecular Nanojunction Photocatalysts for Hydrogen Evolution by Using Automated Screening and Flow Synthesis," *Nature Synthesis* 3 (2024): 595–605, https://doi.org/10.1038/s44160-024-00494-9.

46. J. Xu, Y. He, S. Bi, et al., "An Olefin-Linked Covalent Organic Framework as a Flexible Thin-Film Electrode for a High-Performance Micro-Supercapacitor," *Angewandte Chemie International Edition* 58 (2019): 12065–12069, https://doi.org/10.1002/anie.201905713.

47. J.-S. M. Lee and A. I. Cooper, "Advances in Conjugated Microporous Polymers," *Chemical Reviews* 120 (2020): 2171–2214, https://doi.org/10.1021/acs.chemrev.9b00399.

48. C. Li, J. Liu, H. Li, K. Wu, J. Wang, and Q. Yang, "Covalent Organic Frameworks With High Quantum Efficiency in Sacrificial Photocatalytic Hydrogen Evolution," *Nature Communications* 13 (2022): 2357, https://doi.org/10.1038/s41467-022-30035-x.

49. E. Zhou, X. Zhang, L. Zhu, et al., "Ultrathin Covalent Organic Framework Nanosheets for Enhanced Photocatalytic Water Oxidation," *Science Advances* 10 (2024): eadk8564, https://doi.org/10.1126/sciadv.adk8564.

15213773, 2026, 42, Downloaded from https://onlinelibrary.wiley.com/doi/10.1002/anie.4237539 by Shengqian Ma - University Of North Texas Willis Library , Wiley Online Library on [21/10/2026]. See the Terms and Conditions (https://onlinelibrary.wiley.com/terms-and-conditions) on Wiley Online Library for rules of use; OA articles are governed by the applicable Creative Commons License

50. L. Zhang, C. Wang, Q. Jiang, P. Lyu, and Y. Xu, "Structurally Locked High-Crystalline Covalent Triazine Frameworks Enable Remarkable Overall Photosynthesis of Hydrogen Peroxide," *Journal of the American Chemical Society* 146 (2024): 29943–29954, https://doi.org/10.1021/jacs.4c12339.

51. A. Kong, T. Yang, H. Yan, et al., "Three-Dimensional Bicarbazole-Based Covalent Organic Frameworks as Efficient Yeager-Type Photocatalysts for H_2O_2 Generation in a Two-Phase System," *Journal of the American Chemical Society* 147 (2025): 20855–20864, https://doi.org/10.1021/jacs.5c04447.

52. P. Das, J. Roeser, and A. Thomas, "Solar Light Driven H_2O_2 Production and Selective Oxidations Using a Covalent Organic Framework Photocatalyst Prepared by a Multicomponent Reaction," *Angewandte Chemie International Edition* 62 (2023): e202304349.

53. J. Cheng, S. Wan, and S. Cao, "Promoting Solar-Driven Hydrogen Peroxide Production over Thiazole-Based Conjugated Polymers via Generating and Converting Singlet Oxygen," *Angewandte Chemie International Edition* 62 (2023): e202310476, https://doi.org/10.1002/anie.202310476.

54. M. Kou, Y. Wang, Y. Xu, et al., "Molecularly Engineered Covalent Organic Frameworks for Hydrogen Peroxide Photosynthesis," *Angewandte Chemie International Edition* 61 (2022): e202200413, https://doi.org/10.1002/anie.202200413.

55. Y. Luo, B. Zhang, C. Liu, et al., "Sulfone-Modified Covalent Organic Frameworks Enabling Efficient Photocatalytic Hydrogen Peroxide Generation via One-Step Two-Electron O_2 Reduction," *Angewandte Chemie International Edition* 62 (2023): e202305355, https://doi.org/10.1002/anie.202305355.

56. Y. Ju, H. Lin, G. Tan, et al., "Regulating the Electronic Structure of Covalent Organic Frameworks via Heterocyclic Isomers for Highly Efficient Photocatalytic H_2O_2 Generation," *Nature Communications* 16 (2025): 5658, https://doi.org/10.1038/s41467-025-60960-6.

57. R. Sun, X. Yang, X. Hu, et al., "Unprecedented Photocatalytic Hydrogen Peroxide Production via Covalent Triazine Frameworks Constructed From Fused Building Blocks," *Angewandte Chemie International Edition* 64 (2024): e202416350, https://doi.org/10.1002/anie.202416350.

58. Z. Zhang, Q. Zhang, Y. Hou, et al., "Tris(triazolo)Triazine-Based Covalent Organic Frameworks for Efficiently Photocatalytic Hydrogen Peroxide Production," *Angewandte Chemie International Edition* 63 (2024): e202411546, https://doi.org/10.1002/anie.202411546.

59. W. Zhang, M. Sun, J. Cheng, X. Wu, and H. Xu, "Regulating Electron Distribution in Regioisomeric Covalent Organic Frameworks for Efficient Solar-Driven Hydrogen Peroxide Production," *Advanced Materials* 37 (2025): 2500913, https://doi.org/10.1002/adma.202500913.

60. Q. Wu, J. Cao, X. Wang, et al., "A Metal-Free Photocatalyst for Highly Efficient Hydrogen Peroxide Photoproduction in Real Seawater," *Nature Communications* 12 (2021): 483, https://doi.org/10.1038/s41467-020-20823-8.

61. C. Chu, Z. Chen, D. Yao, X. Liu, M. Cai, and S. Mao, "Large-Scale Continuous and In Situ Photosynthesis of Hydrogen Peroxide by Sulfur-Functionalized Polymer Catalyst for Water Treatment," *Angewandte Chemie International Edition* 63 (2024): e202317214, https://doi.org/10.1002/anie.202317214.

62. A. Chakraborty, A. Alam, U. Pal, et al., "Enhancing Photocatalytic Hydrogen Peroxide Generation by Tuning Hydrazone Linkage Density in Covalent Organic Frameworks," *Nature Communications* 16 (2025): 503, https://doi.org/10.1038/s41467-025-55894-y.

Supporting Information

Additional supporting information can be found online in the Supporting Information section.

Supporting File: anie74330-sup-0001-SuppMat.pdf.

15213773, 2026, 42, Downloaded from https://onlinelibrary.wiley.com/doi/10.1002/anie.4237539 by Shengqian Ma - University Of North Texas Willis Library , Wiley Online Library on [21/10/2026]. See the Terms and Conditions (https://onlinelibrary.wiley.com/terms-and-conditions) on Wiley Online Library for rules of use; OA articles are governed by the applicable Creative Commons License